J. Fluid Mech. (2003), *vol.* 479, *pp.* 125–144. © 2003 Cambridge University Press
DOI: 10.1017/S0022112002003415 Printed in the United Kingdom

Pattern formation in the marginally unstable Ekman layer

By T. M. HAEUSSER[1] AND S. LEIBOVICH[2]

[1]European Patent Office, The Hague

[2]Sibley School of Mechanical and Aerospace Engineering, Cornell University, Ithaca, NY 14853, USA

(Received 5 January 1998 and in revised form 2 October 2002)

We consider the spatio-temporal evolution of patterns in the marginally unstable Ekman layer driven by an applied shear stress. Both the normal and tangential components of the Earth's angular velocity are included in a tangent plane approximation of the oceanic boundary layer at latitude λ. The fluid motion in a layer of finite depth as well as one of infinite depth is considered. The linear instability in the infinite depth case is known to depend on the direction of the applied stress for $\lambda \neq 90°$, but this dependence is weak for the stress-driven Ekman layer. By contrast, the weakly nonlinear motion exhibits for finite and infinite depths qualitatively different dynamics for different stress directions.

The problem is treated by the method of multiple scales. In the case of finite depth, this leads to the Davey–Hocking–Stewartson equation, an amplitude equation of complex Ginzburg–Landau type coupled to a Poisson equation. In the case of infinite depth, it leads to the anisotropic complex Ginzburg–Landau equation for the amplitude of the roll motion. Motions in both finite and infinite depth basins are explored by numerical simulation, and are shown to lead to chaotic dynamics for the modulation envelope in most cases. The statistics and the nature of the patterns produced in this motion are discussed.

1. Introduction

Ekman's (1905) model is the prototype of the planetary boundary layer, and is a basic feature of all motion in a rapidly rotating fluid system (see Greenspan 1968). The Ekman spiral solution to the horizontally homogeneous Ekman layer problem is an exact solution of the Navier–Stokes equations in a rotating frame of reference, assuming a constant (eddy) viscosity. Ekman's solution describes the relative motion in a layer of fluid rotating at angular velocity $\Omega_E|\sin\lambda|$ and confined between two planes normal to the axis of rotation. One of the planes may be removed to infinity, in which case the resulting velocity profiles are of especially simple form. In the geophysical applications contemplated by Ekman, the motion is interpreted as a local one, with one of the boundaries being the tangent plane to the Earth at latitude λ.

Two idealized Ekman layer problems have natural geophysical interpretations, and in both the layer is usually regarded as a half-space. In the first one, the fluid layer above the tangent plane represents the atmosphere, and deviations from rigid-body rotation are driven by horizontally homogeneous winds aloft, with a no-slip ground plane. This atmospheric Ekman layer has received far more attention in the literature than the second problem, in which the tangent plane represents the air–sea interface and the fluid below represents the ocean. The deviation from rigid-body motion in

https://doi.org/10.1017/S0022112002003415 Published online by Cambridge University Press

this case is assumed driven by a horizontally homogeneous applied stress, imagined to be applied by the wind. This problem provided the original impetus for Ekman's work.

Suitably normalized, both steady Ekman layer problems depend only on a Reynolds number $R = u_0 d_0/\nu_T$, where d_0 is the Ekman layer e-folding depth defined in (2.1), u_0 is the scaling speed appropriate to the problem considered, and ν_T is the eddy viscosity. In the atmospheric case, the scaling speed is the geostrophic wind speed aloft and for the oceanic case it is defined in (2.1).

The Ekman spiral solution is unstable when R exceeds a critical value. This was apparently first noted by Stern (1960). The instability was subsequently explored theoretically and numerically for cases with $\lambda = 90°$ (Faller & Kaylor 1966*a*, *b*, 1967; Barcilon 1965; Lilly 1966; Brown 1970; Iooss, Nielsen & True 1978; Melander 1983; Spooner & Criminale 1982; Spooner 1983) when the flow is barotropic and in numerous other papers when the flow is stratified. This case is appropriate for laboratory experiments (which come closest to representing the atmospheric model, see Faller 1963; Faller & Kaylor 1966*a*; Tatro & Mollo-Christensen 1967; Caldwell & Van Atta 1970; Caldwell, Van Atta & Helland 1972). In the laboratory there is no horizontal component of the angular velocity of the experimental apparatus (the traditional approximation), but in the geophysical application the horizontal component cannot be neglected. This was first noted by Wippermann (1969), and the effects of the horizontal component for $\lambda = 45°$N on stability predictions were further explored for both barotropic and stratified atmospheric models in Etling (1971), Etling & Wippermann (1975) and Wippermann, Etling & Kirstein (1978). The variation of the linear stability characteristics for all latitudes for both oceanic and atmospheric barotropic models was considered by Leibovich & Lele (1985).

All linearized stability analyses reveal that the instability arises as a Hopf bifurcation. Iooss *et al.* (1978) also consider the post-bifurcation behaviour for the unstratified, infinite-depth, Ekman layer in the traditional approximation. They consider temporal development of the wave amplitude only, and compute a Landau coefficient showing that the bifurcation is supercritical.

In this paper we look at the spatio-temporal evolution of the weakly nonlinear oceanic Ekman layer model for the complete range of latitudes and for both finite and infinite depths. When spatial modulation is allowed, the post-bifurcation disturbance amplitude is governed by the Davey–Hocking–Stewartson equation system (Davey, Hocking & Stewartson 1974) when the layer has finite depth, and this reduces to a complex Ginzburg–Landau equation when the layer has infinite depth. Our considerations of finite depth layers, which assume no-slip on the bottom plane, require that we compute all linearized stability characteristics before proceeding to the determination of the amplitude equations. The presence of a no-slip bottom in the finite depth calculations is a stabilizing influence, as might be anticipated on heuristic grounds. For example, the critical Reynolds number for $\lambda = 90°$ increases from 11.82 for the infinite depth case to 31.25 for the case of depth approximately $3.16 \times d_0$.

We find that the bifurcation is supercritical for both finite and infinite depths for all considered latitudes. In contrast to most investigations of the pattern forming systems that have employed the complex Ginzburg–Landau equation, the amplitude equations governing the Ekman layer are anisotropic. The nonlinear evolution of patterns is investigated by numerical simulation of the amplitude equations. As in a number of other pattern formation systems, the pattern of rolls representing the motion at bifurcation is perturbed by a collection of spiral and other defects that move through the field, generating alterations of the local wavelength. Even for modest supercritical

https://doi.org/10.1017/S0022112002003415 Published online by Cambridge University Press

conditions, the motion can be chaotic depending on the direction of the applied stress, apparently due to chaotic motion and interaction of defects. This qualitative dependence of the dynamics on wind direction is particularly interesting.

We find that the instability of the Stokes wave solutions of the amplitude equations is a useful guide to the appearance of chaotic dynamics. The statistical characteristics of the chaotic motion, including the density of defects and spatial and temporal correlations, are determined numerically.

The oceanic Ekman layer had not received the same level of attention as given to the atmospheric Ekman layer, at least regarding the possible consequences of instability. This may be due in part to the fact that laboratory experiments modelling the atmospheric boundary layer are more easily done, and it does not appear that attempts have been made to construct a stress-driven Ekman layer in the laboratory. More importantly, the frequent appearance of cloud streets in the atmosphere led to the suggestion that their formation may be due to Ekman layer instability. This suggestion is supported by the resemblance of cloud rows to laboratory visualizations of Ekman layer instability. Much of the work we have cited has addressed this issue. Other evidence from large-eddy (Deardorff 1972; Mason & Thomson 1987) and direct numerical simulations (Coleman, Ferziger & Spalart 1990) of turbulent Ekman layers is counterindicative, showing no substantial tendency to form large-scale structures in neutrally stratified fluid. Such structures are found in simulations with unstable stratification, thus lending weight to the view that cloud streets are due to thermal instability organized by wind shear.

The oceanic boundary layer also has a strong visual counterpart to cloud streets in the form of elongated rolls or windrows known as Langmuir circulation. Ekman layer instability also has been invoked as a possible cause for these features (Faller 1964). This view has also now been discredited, and a mechanism that has mathematical analogies to thermal instability but is mechanical in origin is now believed to be the origin of the Langmuir circulation (see, for example, Leibovich 1983; Smith 1996).

Thus, in both the atmospheric and oceanic cases, the observed visible pattern seems to be due to an instability that does not owe its existence directly to the properties of the Coriolis acceleration, although the phenomena are embedded in the Ekman layer and presumably influenced by this embedding. In fact, it was our intention of exploring this interacting Ekman layer/Langmuir circulation instability that led us to this study as a preliminary when it became clear that little was known about the pattern formation characteristics of the weakly nonlinear Ekman layer. The results have proven to be intrinsically interesting in the general context of pattern formation in fluid systems.

2. Problem formulation

2.1. *Navier–Stokes equations and basic state*

We consider the motion of a layer of water on the Earth at latitude λ in the tangent plane approximation. The layer has constant depth h, which is taken to be infinite in parts of the analysis. The water density ρ is constant and the effects of small-scale turbulence are parameterized by a constant eddy viscosity ν_T. The wind exerts a stress on the water surface, which is in a direction θ north of east and has magnitude τ. The coordinate system is chosen to rotate with the Earth, with x_3-axis (unit vector $\hat{\boldsymbol{e}}_3$) normal to the tangent plane and pointing upwards. The x_1-axis is in the direction of the surface stress and the x_2-axis completes the right-handed Cartesian coordinate system. The plane $x_3 = 0$ coincides with the water surface.

https://doi.org/10.1017/S0022112002003415 Published online by Cambridge University Press

We consider non-zero latitudes and introduce non-dimensional variables with unit length d_0 and unit speed u_0 given by

$$d_0 = \left(\frac{\nu_T}{\Omega_E|\sin\lambda|}\right)^{1/2}, \qquad u_0 = \frac{\tau}{\rho(2\nu_T\Omega_E|\sin\lambda|)^{1/2}}, \tag{2.1}$$

where Ω_E is the magnitude of the Earth's angular velocity. The incompressible approximations of the momentum and continuity equations take the form

$$(\partial_t + \boldsymbol{u}\cdot\nabla)\boldsymbol{u} = -\nabla p - 2\boldsymbol{\Omega}\times\boldsymbol{u} + \frac{1}{R}\Delta\boldsymbol{u}, \tag{2.2a}$$

$$\nabla\cdot\boldsymbol{u} = 0, \tag{2.2b}$$

where $\boldsymbol{u}$ is the velocity, p the modified pressure, and

$$\boldsymbol{\Omega} = \frac{\operatorname{sign}\lambda}{R}(\cot\lambda\,\sin\theta,\ \cot\lambda\,\cos\theta,\ 1). \tag{2.3}$$

The Reynolds number $R = u_0 d_0/\nu_T$ is the control parameter. The boundary conditions are zero vertical velocity and constant horizontal stress at $x_3 = 0$, and no slip at $x_3 = -h$:

$$u_3 = \partial_3 u_1 - 2^{1/2} = \partial_3 u_2 = 0 \quad \text{at } x_3 = 0, \tag{2.4a}$$

$$\boldsymbol{u} = \boldsymbol{0} \quad \text{at } x_3 = -h. \tag{2.4b}$$

We discuss only northern latitudes ($0^\circ < \lambda \leqslant 90^\circ$), since results for the southern hemisphere can be found from this information via the following symmetry of equations (2.2) and boundary conditions (2.4):

$$(\lambda,\ \theta,\ x_2,\ u_2) \to (-\lambda,\ -\theta,\ -x_2,\ -u_2). \tag{2.5}$$

Equations (2.2) with boundary conditions (2.4) have a simple solution that constitutes a balance between the Coriolis force and the friction force. In complex notation Ekman's solution is

$$U_1 + \mathrm{i}\,U_2 = \exp\left(-\frac{\mathrm{i}\pi}{4}\right)\frac{\sinh(1+\mathrm{i})(x_3+h)}{\cosh(1+\mathrm{i})h}. \tag{2.6}$$

This solution is the basic state whose instability and subsequent nonlinear evolution we investigate. In the limit $h \to \infty$, it takes the form of a logarithmic spiral with surface velocity at an angle of 45° to the right of the wind direction. At finite depths the surface velocity is more nearly aligned with the wind, and for $h \to 0$ the flow tends to Couette flow aligned with the wind direction:

$$U_1 + \mathrm{i}\,U_2 \to \exp(x_3)\left\{\cos\left(x_3 - \tfrac{1}{4}\pi\right) + \mathrm{i}\,\sin\left(x_3 - \tfrac{1}{4}\pi\right)\right\} \quad \text{as } h \to \infty, \tag{2.7a}$$

$$U_1 + \mathrm{i}\,U_2 \to 2^{1/2}\,(x_3 + h) \quad \text{as } h \to 0. \tag{2.7b}$$

2.2. *Perturbation equations*

We decompose the velocity as $\boldsymbol{u} = \boldsymbol{U} + \boldsymbol{v}$ and the pressure as $p = P + \pi$, where P is the pressure belonging to the basic state $\boldsymbol{U}$ given in (2.6). We have found it convenient to use an augmented poloidal–toroidal representation for the solenoidal vector field $\boldsymbol{v}$. The poloidal–toroidal decomposition is a general representation for

https://doi.org/10.1017/S0022112002003415 Published online by Cambridge University Press

solenoidal vector fields that are spatially periodic in the unbounded directions in a layer (Joseph 1976). This is assumed the case here at lowest order, but mean flows can develop at higher order and the representation needs to be augmented. We have done this by appending a vector field $\boldsymbol{G}$ to account for those parts of the velocity vector that are not periodic. Thus the perturbation velocity is expanded as

$$\boldsymbol{v} = \nabla \times (\nabla \times \chi\, \hat{\boldsymbol{e}}_3) + \nabla \times \psi\, \hat{\boldsymbol{e}}_3 + \boldsymbol{G}, \tag{2.8}$$

where χ and ψ are scalar fields. The standard multiple-scale analysis described in more detail in Appendix B, formally introduces slow and fast horizontal spatial scales. This leads to potentials χ and ψ that are periodic in the fast horizontal variables, and are modulated by an amplitude function varying on the slow scale. The vector field $\boldsymbol{G}$ depends on horizontal coordinates only through slow variables. Equations for χ and ψ are obtained by operating with $\hat{\boldsymbol{e}}_3 \cdot \nabla \times \nabla \times$ and $\hat{\boldsymbol{e}}_3 \cdot \nabla \times$ on the momentum equation. This results in the equations

$$(\partial_t + U_\mu \partial_\mu)\Delta\Delta_h\chi = U_\mu'' \partial_\mu \Delta_h \chi - 2\Omega_j \partial_j \Delta_h \psi + \frac{1}{R}\Delta^2 \Delta_h \chi - \partial_{13}(v_j \partial_j v_1) - \partial_{23}(v_j \partial_j v_2) + \Delta_h (v_j \partial_j v_3), \tag{2.9a}$$

$$(\partial_t + U_\mu \partial_\mu)\Delta_h\psi = (U_1' \partial_2 - U_2' \partial_1)\Delta_h \chi + 2\Omega_j \partial_j \Delta_h \chi + \frac{1}{R}\Delta\Delta_h \psi - \partial_2 (v_j \partial_j v_1) + \partial_1 (v_j \partial_j v_2). \tag{2.9b}$$

Here and subsequently, Latin indices run from 1 to 3, Greek indices run from 1 to 2, and repeated indices are summed over. The horizontal Laplacian operator is denoted by Δ_h and prime denotes the derivative with respect to x_3. Equations for $\boldsymbol{G}$ are obtained by averaging the momentum equation over the fast horizontal variables. The averaging operator is represented by the symbol $\langle \ldots \rangle_h$. The horizontal components of the resulting equation are

$$\partial_t G_1 + G_3 U_1' = -\langle \partial_1 \pi \rangle_h - 2\Omega_2 G_3 + 2\Omega_3 G_2 + R^{-1} \partial_{33} G_1 - \partial_3 \langle v_1 v_3 \rangle_h, \tag{2.10a}$$

$$\partial_t G_2 + G_3 U_2' = -\langle \partial_2 \pi \rangle_h - 2\Omega_3 G_1 + 2\Omega_1 G_3 + R^{-1} \partial_{33} G_2 - \partial_3 \langle v_2 v_3 \rangle_h. \tag{2.10b}$$

Boundary conditions for χ, ψ and $\boldsymbol{G}$ follow from the boundary conditions for $\boldsymbol{v}$ (equations (2.4) without the inhomogeneous term) and the definition (2.8).

3. Linear instability

Suppose we fix the depth h, the latitude λ, and the wind stress direction θ. Then, as the Reynolds number R passes the critical value R_c, the basic state becomes unstable to infinitesimal periodic perturbations of wavenumber vector $\boldsymbol{k}_c$ and angular frequency ω_c, and these critical parameters of the instability are functions of h, λ and θ. Except for $\lambda = 90°$, the Earth's angular velocity has a horizontal component, and that causes the dependence of the parameters on λ and θ. The critical Reynolds number at each latitude has a minimum over wind direction θ, and this defines the most dangerous wind direction for the initialization of instability. The linear instability of the infinite depth case has been explored by Leibovich & Lele (1985), with most attention paid to the direction of wind stress that is most favourable to instability. Here we are interested in the effect of wind direction on the nature of the motions that ensue at each latitude. We therefore recompute the linear stability characteristics with this goal in mind. We are not aware of linearized stability computations for

https://doi.org/10.1017/S0022112002003415 Published online by Cambridge University Press

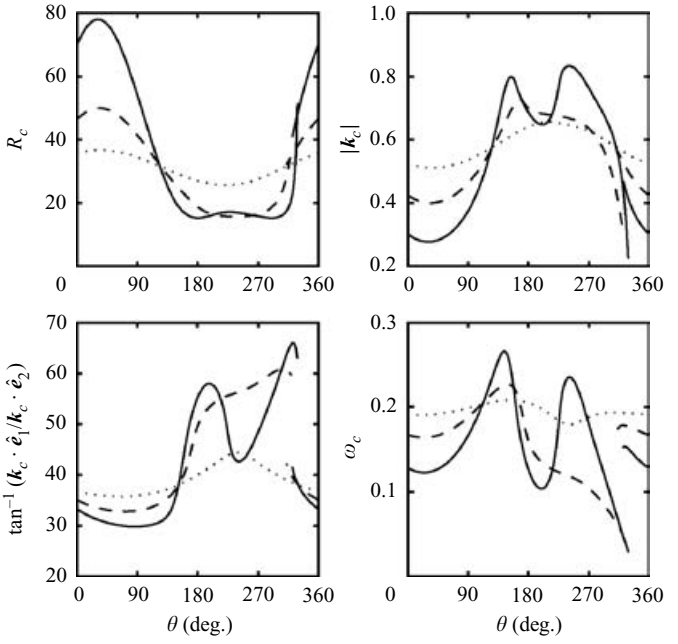


FIGURE 1. Critical parameters for the depth $h = 0.1^{-1/2}$ and the latitudes $\lambda = 20^\circ$ (solid), 40° (broken) and 70° (dotted).

finite depth cases, and so we calculate stability parameters for one choice of finite depth.

Numerical values of the critical parameters for selected values of h, λ and θ are given in Appendix A. Figures 1 and 2 show the critical parameters for the depth $h = 0.1^{-1/2} \approx 3.16$ and for infinite depth respectively. For $h = 0.1^{-1/2}$ the parameters are shown as functions of θ for $\lambda = 20^\circ$, 40° and 70°. For infinite depth they are shown for $\lambda = 40^\circ$ and 70°. The dependence of the parameters on θ is stronger for lower latitudes, because the horizontal component of the Earth's angular velocity is larger at lower latitudes. Furthermore, the finite depth is seen to have a stabilizing effect on the Ekman layer, since R_c is increased substantially compared to the infinite depth case. This is expected, since with decreasing depth the basic state approaches the linear Couette flow profile, which is known to be linearly stable at all Reynolds numbers. The value $h = 0.1^{-1/2}$ is chosen to be small enough that the corresponding basic state is still unstable.

In the case $h = 0.1^{-1/2}$, the parameters $\boldsymbol{k}_c$ and ω_c are discontinuous for $\lambda = 20^\circ$ (at $\theta = 328^\circ$) and $\lambda = 40^\circ$ (at $\theta = 317^\circ$). This is because for these latitudes there are two minima on the marginal stability surfaces for an interval of wind directions. One of these minima passes the other at the indicated angle, i.e. at the discontinuity there is a bifurcation point of codimension 2.

4. Amplitude equations

We use perturbation theory with expansion parameter $\epsilon = [(R - R_c)/R_c]^{1/2}$ to investigate the dynamics of the Ekman layer slightly above the instability threshold and use the method of multiple scales to eliminate secular terms. At first order in ϵ, equations (2.9) determine the critical parameters R_c, $\boldsymbol{k}_c$ and ω_c. At second order,

https://doi.org/10.1017/S0022112002003415 Published online by Cambridge University Press

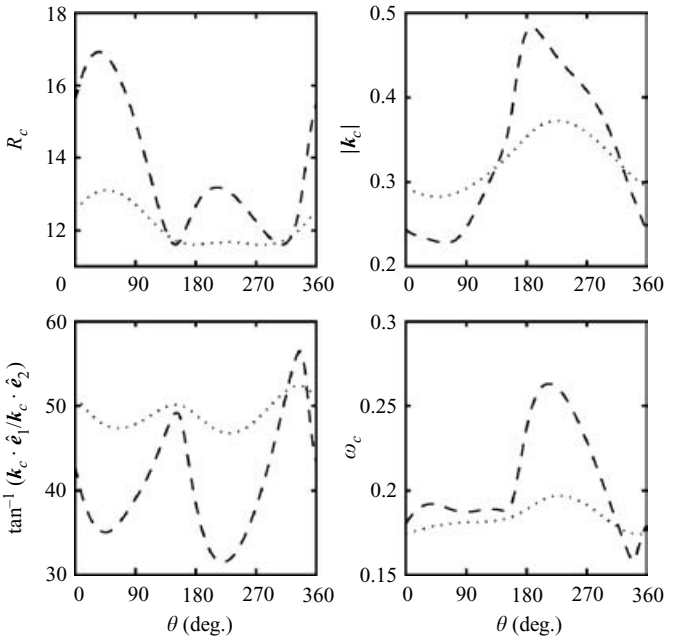


FIGURE 2. Critical parameters for infinite depth and the latitudes $\lambda = 40°$ (broken) and $70°$ (dotted).

a solvability condition of (2.9) determines the group velocity $\boldsymbol{c}_g$ in (4.1). At third order, a solvability condition of (2.9) yields a differential equation for the complex amplitude a of the unstable mode. Details of the definitions and calculations are given in Appendix B. We do not explore the interaction of the two unstable modes at points in parameter space where the bifurcation has codimension 2, and our weakly nonlinear analysis is therefore incomplete at those points.

4.1. *Finite depth*

In the finite depth case, the amplitude equation is coupled to a Poisson equation for the real pressure variable p_s that drives a mean flow. That flow ensures that the boundary condition of zero vertical velocity at the lower boundary is satisfied at third order. The pressure equation is obtained by integrating the third-order continuity equation over the vertical coordinate. The resulting equations are the Davey–Hocking–Stewartson equations (Davey *et al.* 1974)

$$(\partial_t + \boldsymbol{c}_g \cdot \boldsymbol{e}_\mu \partial_\mu)\, a = \left\{ c_r \left(\frac{R}{R_c} - 1 \right) + c_{\mu\nu} \partial_{\mu\nu} + c_\mu \partial_\mu p_s - c_a |a|^2 \right\} a, \tag{4.1a}$$

$$(\partial_{11} + \partial_{22})\, p_s = f_\mu \partial_\mu |a|^2, \tag{4.1b}$$

where as before repeated Greek indices are summed from 1 to 2. The coefficients f_μ and the components of the group velocity vector $\boldsymbol{c}_g$ are real constants and the other coefficients are complex constants. Like the critical parameters, all coefficients in (4.1) are functions of h, λ and θ, and must be computed. Numerical values of the coefficients in equations (4.1) for the depth $h = 0.1^{-1/2}$, and for selected values of λ and θ are given in table 1 of Appendix A.

https://doi.org/10.1017/S0022112002003415 Published online by Cambridge University Press

Equations (4.1) are invariant under the transformation

$$\left(\frac{R}{R_c}-1,\ t,\ x_\mu,\ a\right)\rightarrow\left(s\left(\frac{R}{R_c}-1\right),\ \frac{t}{s},\ \frac{x_\mu}{s^{1/2}},\ s^{1/2}\,a\right), \tag{4.2a}$$

$$p_s\rightarrow s^{1/2}\,p_s, \tag{4.2b}$$

for any real and positive parameter s. Hence one can find a solution of equations (4.1) for a fixed value of R and use (4.2) to obtain solutions corresponding to other values. This procedure does not yield solutions for the physical problem for all values of R, however, because of the associated rescaling of the system size.

A complete reduction of equations (4.1) to an irreducible form is effected by a Galilean transformation, a rescaling of time, distance and amplitude, and a shift in frequency. This results in the equations

$$\begin{aligned}\partial_t\,a=\{1+(1+\mathrm{i}\check{c}_{11})\partial_{11}+(\hat{c}_{12}+\mathrm{i}\check{c}_{12})\partial_{12}+(\hat{c}_{22}+\mathrm{i}\check{c}_{22})\partial_{22}\\ +(1+\mathrm{i}\check{c}_1)\partial_1 p_s+(\hat{c}_2+\mathrm{i}\check{c}_2)\partial_2 p_s-(1+\mathrm{i}\check{c}_a)|a|^2\}\,a,\end{aligned} \tag{4.3a}$$

$$(\partial_{11}+\partial_{22})\,p_s=(\hat{f}_1\partial_1+\hat{f}_2\partial_2)|a|^2, \tag{4.3b}$$

which contain the 11 real parameters $\hat{c}_{11}$, $\check{c}_{12}$, etc. We give this reduction to an irreducible form only for completeness and will not use equations (4.3) hereafter.

4.2. *Infinite depth*

In the infinite depth case, no pressure variable is needed to ensure zero vertical velocity at infinite depth. The evolution of the complex amplitude a is described by the complex Ginzburg–Landau equation

$$(\partial_t+\boldsymbol{c}_g\cdot\boldsymbol{e}_\mu\partial_\mu)\,a=\left\{c_r\left(\frac{R}{R_c}-1\right)+c_{\mu\nu}\partial_{\mu\nu}-c_a|a|^2\right\}a, \tag{4.4}$$

where again the components of the group velocity vector $\boldsymbol{c}_g$ are real constants and the other coefficients are complex constants. Numerical values of the coefficients in equation (4.1) for selected values of λ and θ are shown in table 2 of Appendix A. Again, transformation (4.2a) leaves (4.4) invariant. Furthermore, a Galilean transformation and a general non-orthogonal coordinate transformation, plus a rescaling of time and amplitude, and a shift in frequency, i.e.

$$(t,\ x_\mu,\ a)\rightarrow(s_t t,\ H_{\mu\nu}x_\nu-\boldsymbol{c}_g\cdot\boldsymbol{e}_\mu t,\ s_a a\exp(\mathrm{i}\,s_\omega s_t t)), \tag{4.5}$$

transform (4.4) into the irreducible form

$$\partial_t\,a=\{1+(1+\mathrm{i}\,b_1)\partial_{11}+(1+\mathrm{i}\,b_2)\partial_{22}-(1+\mathrm{i}\,c)|a|^2\}\,a, \tag{4.6}$$

which depends only on the three real parameters b_1, b_2 and c. These constants are functions of λ and θ (the depth being infinite) and must again be computed. Samples of the values of these coefficients are given in table 2.

5. Stokes wave solutions of the amplitude equations

5.1. *Finite depth*

Equations (4.1) describe patterns in the marginally unstable Ekman layer in the finite depth case. They have simple nonlinear plane wave solutions of the form

$$a=F\exp(\mathrm{i}\,\boldsymbol{Q}\cdot\boldsymbol{x}+\mathrm{i}\,\Omega t), \tag{5.1a}$$

$$p_s=0, \tag{5.1b}$$

https://doi.org/10.1017/S0022112002003415 Published online by Cambridge University Press

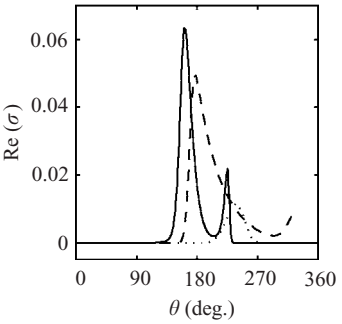


FIGURE 3. Growth rate of the most unstable perturbation of the homogeneous solution $\boldsymbol{Q} = \boldsymbol{0}$ for $h = 0.1^{-1/2}$, $R = 2 \times R_c$ and the latitudes $\lambda = 20°$ (solid), $40°$ (broken) and $70°$ (dotted).

where the real constants F and Ω can be easily found in terms of the horizontal wavenumber vector $\boldsymbol{Q}$ and the coefficients in the equations. All computations in this section are for the choice $R = 2 \times R_c$, where R_c is the critical Reynolds number belonging to the values of h, λ and θ in question. We study the stability of these 'Stokes wave solutions' by substituting

$$a = (F + \delta a_+ \exp(\mathrm{i}\,\boldsymbol{q}\cdot\boldsymbol{x} + \sigma t) + \delta a_- \exp(-\mathrm{i}\,\boldsymbol{q}\cdot\boldsymbol{x} + \sigma^* t)) \exp(\mathrm{i}\,\boldsymbol{Q}\cdot\boldsymbol{x} + \mathrm{i}\,\Omega t) \qquad (5.2a)$$

$$p_s = \delta p_s \exp(\mathrm{i}\,\boldsymbol{q}\cdot\boldsymbol{x} + \sigma t) + \text{c.c.} \qquad (5.2b)$$

into (4.1) and linearizing in the perturbation constants δa_+, δa_- and δp_s. The solution is stable if the growth rate $\mathrm{Re}(\sigma)$ of perturbations for any wavenumber vector $\boldsymbol{q}$, is zero or negative. In figure 3 we show the growth rate of the most unstable perturbation of the homogeneous solution $\boldsymbol{Q} = \boldsymbol{0}$ as a function of θ for $h = 0.1^{-1/2}$ and the latitudes $\lambda = 20°$, $40°$ and $70°$. At all three latitudes, there is an interval of wind directions for which the growth rate is positive, implying that the homogeneous solution is unstable in that interval. For $\lambda = 20°$, $40°$ and $70°$, this interval is [114°, 231°], [156°, 317°] and [196°, 264°], respectively. We therefore expect that the dynamics of the unstable Ekman layer in a finite depth layer depends on the wind direction, the dynamics being more irregular in the interval of instability.

5.2. *Infinite depth*

In the infinite depth case, equation (4.4) is the amplitude equation describing pattern formation in the marginally unstable Ekman layer. As described above, this equation can be transformed into the irreducible form (4.6). Equation (4.4) and equation (4.6) have nonlinear Stokes wave solutions of the form (5.1*b*). Here we will provide results in terms of the amplitude equation in the irreducible form (4.6).

Figure 4 shows the coefficients in (4.6) as functions of θ for $\lambda = 40°$ and $\lambda = 70°$ (the depth being infinite). Instead of b_1 and b_1, we show the 'Benjamin–Feir numbers' $(1 + b_1 c)$ and $(1 + b_2 c)$. If both Benjamin–Feir numbers are positive, there are Stokes wave solutions of equation (4.6) that are stable with respect to long-wavelength modulations. If one or both of the Benjamin–Feir numbers are negative, there are no stable Stokes wave solutions (Benjamin & Feir 1967; Weber, Bodenschatz & Kramer 1991). We see that for $\lambda = 70°$, there are no wind directions for which stable Stokes wave solutions exist. For $\lambda = 40°$ on the other hand, stable Stokes wave solutions exist for wind directions in the interval [210°, 276°]. As in the finite depth case, we

https://doi.org/10.1017/S0022112002003415 Published online by Cambridge University Press

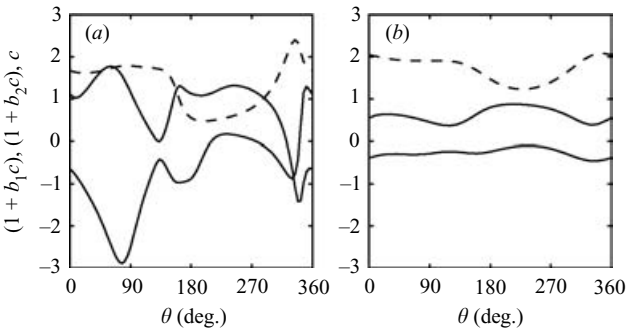


FIGURE 4. Coefficients in the amplitude equation in irreducible form (4.6) for the two latitudes $\lambda = 40°$ (*a*) and 70° (*b*). The Benjamin–Feir numbers $(1+b_2c)$ and $(1+b_2c)$ are shown as solid lines, and the coefficient c is shown as a broken line.

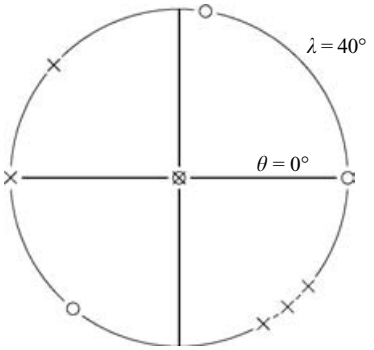


FIGURE 5. Simulations of the amplitude and mean drift equations (4.1) (for finite depth) and of the amplitude equation (4.4) (for infinite depth) are performed with coefficients corresponding to the values of h, λ and θ shown here. The radial coordinate gives $90° - \lambda$ in degrees and the azimuthal coordinate gives θ in degrees. Crosses stand for $h = 0.1^{-1/2}$ and circles stand for infinite depth.

expect the dynamics of the unstable Ekman layer in infinite depth layers to depend on the wind direction, the dynamics being more regular in the interval of stability.

6. Simulations of the amplitude equations

We perform numerical simulations of the amplitude and mean drift equations (4.1) and of the amplitude equation (4.4) to investigate the dynamics of the marginally unstable Ekman layer in finite and infinite depth layers respectively. Details of the initial conditions and duration of the simulations is given in Appendix C.

The simulations are done in the frame moving at group velocity $\boldsymbol{c}_g$. The simulations are performed with coefficients corresponding to the values of h, λ and θ shown in figure 5, and usually with $R = 2 \times R_c$, where R_c is the critical Reynolds number belonging to the values of h, λ and θ in question. Solutions corresponding to other values of R can be obtained from these simulations via transformation (4.2), which also changes the scales of length, time and amplitude. In figure 5, crosses correspond to the finite depth $h = 0.1^{-1/2}$ and circles correspond to infinite depth.

Most simulations exhibit defects, i.e. points at which the magnitude of the complex amplitude a vanishes. At the location of a defect a phase contour along which the real

https://doi.org/10.1017/S0022112002003415 Published online by Cambridge University Press

part of a vanishes crosses one along which the imaginary part vanishes. The phase of a changes by $\pm 2\pi$ as a defect is circled in an anti-clockwise direction. Depending on the sign of the phase change, the defect is said to have positive or negative 'charge'. Defects of opposite charge are created and annihilated pairwise and typically move through the box, disorganizing the field (Coullet, Gil & Lega 1989). In terms of phase contours, a defect pair is created when a loop of a $\mathrm{Re}(a) = 0$ phase contour crosses an $\mathrm{Im}(a) = 0$ contour. In order to characterize the simulated states, we calculate time series of defect numbers and defect speed statistics. Furthermore, we calculate temporal and spatial phase correlation functions as defined by Shraiman *et al.* (1992):

$$C(x_1, x_2, t) = \frac{1}{TL_1L_2} \int_0^T \mathrm{d}t' \int_0^{L_1} \mathrm{d}x_1' \int_0^{L_2} \mathrm{d}x_2' \times \exp(\phi(x_1', x_2', t') - \phi(x_1' + x_1, x_2' + x_2, t' + t)). \quad (6.1)$$

As noted above, most simulations are for Reynolds number $R = 2 \times R_c$, with the understanding that the solutions for all other values of R, in particular those closer to threshold, can be found from these results via the symmetry transformation (4.2). As previously explained, however, the transformation does not produce all solutions for all values of R – there is a size effect. We therefore perform some simulations for values of R different from $2 \times R_c$. In particular, for coefficients corresponding to $h = 0.1^{-1/2}$, $\lambda = 40^\circ$ and $\theta = 138^\circ$, we perform calculations for $R/R_c = 1.01$, 1.1, 1.2, 1.3, 1.5 and 2 in a box of size 316×316 units of length. We observe a transition from regular to chaotic behaviour as R is increased. For $R = 1.01 \times R_c$, the simulation tends to the homogeneous Stokes wave solution, which is of course characterized by perfect spatial correlations across the whole box and perfect temporal correlations over arbitrarily long times. For $R/R_c = 1.1$ and 1.2 we observe that the simulations tend to a state which consists of four and eight spiral defects, respectively, that move very slowly. These states are characterized by exponentially decaying spatial correlations, and Gaussian temporal correlations. A comparison of the correlation times, correlation lengths and amplitudes of the results of the simulations for $R/R_c = 1.3$, 1.5 and 2 indicates that they are indeed related to each other by the transformation (4.2)

6.1. *Finite depth*

All finite depth simulations with $R = 2 \times R_c$ yield chaotic solutions with defects present. The following description of results focuses on two cases: simulations with coefficients corresponding to $h = 0.1^{-1/2}$, $\lambda = 40^\circ$, $\theta = 180^\circ$ and $R = 2 \times R_c$ are referred to as 'case I', and simulations with coefficients corresponding to $h = 0.1^{-1/2}$, $\lambda = 40^\circ$, $\theta = 138^\circ$ and $R = 2 \times R_c$ are referred to as 'case II'. Figure 6 shows snapshots of simulations of case I and case II. The two top figures give the results for case I and those at the bottom for case II. The left figures show lines of constant phase of the amplitude a. The right figures show the corresponding states of a physical field. Positive values are shown in black and negative values in white.

In case II some defects appear as pronounced spirals. These are long-lived structures as can be seen from figure 7, which shows defect tracks, indicating defects of positive (negative) charge by plus- (minus-) signs. The tracks are shown in the frame moving with the group velocity $\boldsymbol{c}_g$ relative to the original frame. The initial state is that shown in figure 6 and the defects are shown at 50 evenly spaced instances spanning a total time interval of 3520 time units. Comparing figures 6 and 7, one can see that some spiral defects are nearly stationary and maintain their identity over the time interval for which the defect tracks are plotted. Since the spirals are shown in the moving

https://doi.org/10.1017/S0022112002003415 Published online by Cambridge University Press

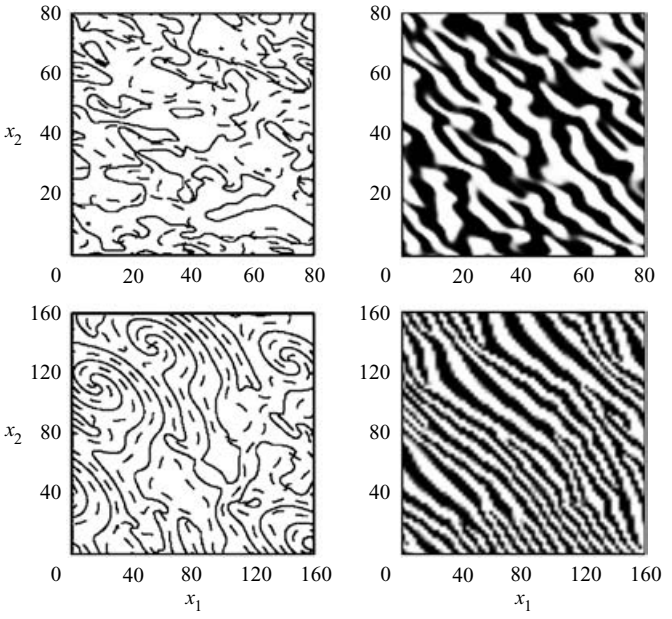


FIGURE 6. Snapshot of a case I simulation (top figures) and of a case II simulation (bottom figures). Lines of constant phase of the amplitude a are shown on the left; the real (imaginary) part of a vanishes along solid (broken) lines. The corresponding state of a physical field is shown on the right; black regions correspond to positive values of the field and white regions to negative values. Note that the area shown for case II is four times that shown for case I. The surface stress is in the x_1-direction.

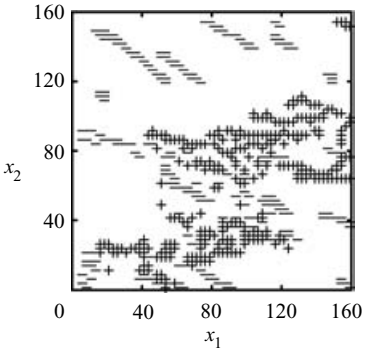


FIGURE 7. Defect tracks for case II, showing defects of positive charge as plus-signs and defects of negative charge as minus-signs. The defects are tracked for a time interval of 3520 time units, starting from the state shown in figure 6.

frame, this means that they travel effectively with velocity $\boldsymbol{c}_g$ in the original frame of reference. Furthermore, all spirals have negative charge, which is presumably a consequence of the broken chiral symmetry due to the rotation of the coordinate system. Indeed, the sign of the charge is reversed under the symmetry transformation (2.5), so that in the solution for the southern hemisphere, generated from case II via (2.5), all spirals have positive charge (as has previously been mentioned earlier in this section). Pronounced spirals are also present in simulations with coefficients corresponding to $h = 0.1^{-1/2}$, $\lambda = 40°$, $\theta = 320°$, and $h = 0.1^{-1/2}$, $\lambda = 90°$. Note that

https://doi.org/10.1017/S0022112002003415 Published online by Cambridge University Press

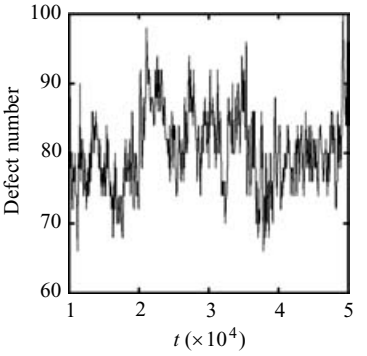


FIGURE 8. Time series of the defect number in a box of size 316×316 for case II.

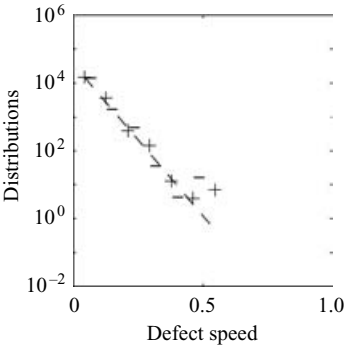


FIGURE 9. Distributions of defect speeds for case II. The distributions for defects with positive (negative) charge are shown as plus-signs (minus-signs) and are not normalized. The broken line is an exponential fit and has e-folding speed 0.05.

the total charge for a periodic system vanishes, so positive charges in the northern hemisphere do not appear as spirals, but merely as intersections of contours of real and imaginary parts of a.

In all finite depth simulations, the defect number varies erratically with time. Figure 8 shows the time series of defect numbers for case II in a box of size 316×316. Time series of simulations with other coefficients have a similar form. The average defect density depends strongly on the coefficients in equations (4.1). It is highest in case I with on average about 0.007 defects per unit area, and is on average about 9 times lower in case II.

We calculate the distributions of defect speeds for several simulations and find them to be roughly exponential. Figure 9 shows the speed distributions of defects with positive charge (plus-signs) and negative charge (minus-signs) for case II. In order to generate these distributions, we calculate the average absolute speed of a defect over the course of its life and then weight that speed by the lifetime of the defect. The distributions are not normalized. Also shown is an exponential fit to these distributions; the e-folding speed for this fit is about 0.05.

Finally, we calculate spatial and temporal phase correlation functions. In all finite depth calculations, both correlations decay roughly exponentially, although with very different time and length scales. The temporal phase correlation functions

https://doi.org/10.1017/S0022112002003415 Published online by Cambridge University Press

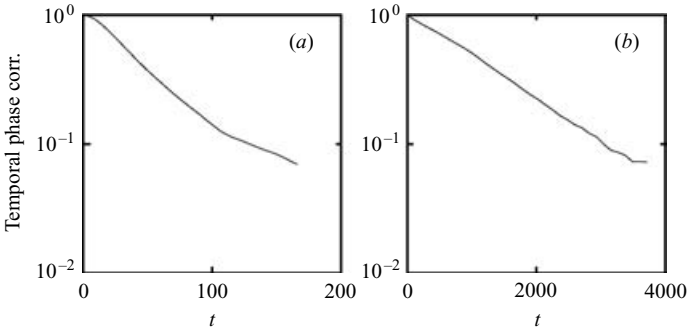


FIGURE 10. Temporal phase correlation function for case I (*a*) and case II (*b*).

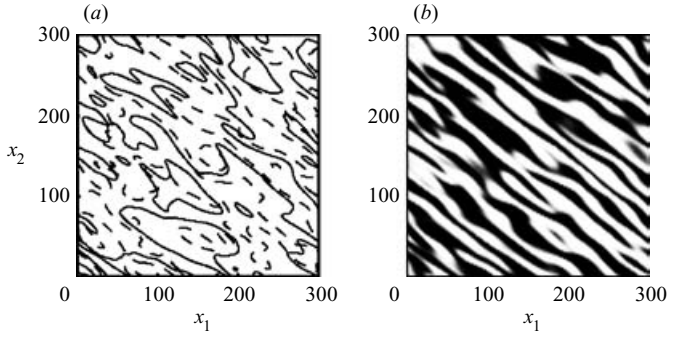


FIGURE 11. Snapshot of a case III simulation. Lines of constant phase of the amplitude a are shown in (*a*); the real (imaginary) part of a vanishes along solid (broken) lines. The corresponding state of a physical field is shown in (*b*); black regions correspond to positive values of the field and white regions to negative values. The surface stress is in the x_1-direction.

for cases I and II are shown in figure 10. Note the different time scales in the two plots.

6.2. *Infinite depth*

Here we focus on results for simulations with coefficients corresponding to $\lambda = 40°$, $\theta = 81°$ and $R = 2 \times R_c$ (case III) and $\lambda = 40°$, $\theta = 231°$ and $R = 2 \times R_c$ (case IV). Figure 11 shows a snapshot of a case III simulation. Figure 11(*a*) shows lines of constant phase of the amplitude a and figure 11(*b*) shows the corresponding state of a physical field. Positive values of that field are shown in black and negative values in white. The simulation of case IV converges to the homogeneous solution $\boldsymbol{Q} = \boldsymbol{0}$ described in the previous section, and is the only simulation corresponding to $R = 2 \times R_c$ that is not chaotic. The amplitude a in this case is constant across the box at any time and the physical fields are perfectly sinusoidal.

7. Discussion and conclusion

The stability of Stokes wave solutions provides some guidance for the actual evolution of the amplitude. For example, the defect density is highest and the temporal phase correlation function has shortest time scale in the simulations of case I,

https://doi.org/10.1017/S0022112002003415 Published online by Cambridge University Press

for which the homogeneous Stokes wave solution is most unstable (see figure 3). Further, the simulations of case IV, for which the corresponding Benjamin–Feir numbers are both positive, tend to the regular homogeneous Stokes wave solution. However, we also observe chaotic solutions when Stokes waves are stable, e.g. in case II the homogeneous solution is stable (see figure 3) but case II simulations are chaotic. A referee has pointed out that similar behaviour has been observed for the isotropic complex Ginsburg–Landau equation and has been attributed to the Eckhaus instability of the spiral waves.

The results we obtained for the temporal phase correlations, the defect speed statistics and the defect densities, are consistent with the notion that the motion of the defects causes the decay in the temporal phase correlations (Coullet *et al.* 1989). This follows from the observation that the average defect distance, as determined from the defect densities, divided by the e-folding decay time of the phase correlations is roughly equal to a typical defect speed in cases I, II and III.

The wind stress τ determines not only the velocity scale u_0, but also the eddy viscosity ν_T, and therefore the length scale d_0. For moderate wind speeds of 10—15 m s^{-1}, reasonable estimates of these quantities are $u_0 \approx 0.05\,\mathrm{m\,s^{-1}}$, $\nu_T \approx 0.015\,\mathrm{m^2\,s^{-1}}$ and $d_0 \approx 15\,\mathrm{m}$. This leads to $R \approx 50$, which is of the same order as R_c in Figures 1 and 2. The results of this paper therefore have relevance for the oceanic Ekman layer under realizable environmental conditions. Our finite depth calculations, for which $h = 0.1^{-1/2}$, correspond in this scenario to a layer depth of about 47 m. With $|\boldsymbol{k}_c| \approx 0.6$, and $\omega_c \approx 0.2$ (see figure 1), the rolls have then a wavelength of $(2\pi/|\boldsymbol{k}_c|)\,d_0 \approx 160\,\mathrm{m}$ and a phase speed of $(\omega_c/|\boldsymbol{k}_c|)u_0 \approx 0.03\,\mathrm{m\,s^{-1}}$. They travel at that phase speed towards smaller values of x_2.

We close by pointing out several caveats that have to be borne in mind. First, we have taken a simplified view of the small-scale turbulence by parameterizing it with a constant eddy viscosity. Second, we performed a secondary stability analysis of the rolls in the Ekman layer (not published), and found that secondary instabilities set in at Reynolds numbers less than 1% above the linear instability threshold. Nevertheless, simulations with coefficients in the stable regime may produce chaotic results. Lastly, and most importantly for application to the ocean, the effect of surface waves – always present under wind forcing – is neglected. These lead to Langmuir circulation, as discussed in the introduction, which are expected to dominate. We have explored the inclusion of Langmuir effects, and shall present the results in another paper.

We wish to thank Eberhard Bodenschatz for many useful conversations and Eberhard Bodenschatz and Bruce Roberts for allowing us to use and to modify their complex Ginzburg–Landau equation simulation code. Thomas Haeusser is grateful for conversations with Professor F. Busse and Professor W. Pesch, and for their hospitality during a visit to Bayreuth. This work was supported by ONR contract N00014-93-1-0476, and NSF grant DMR-9705410.

Appendix A. Coefficients in the amplitude equations

Table 1 shows the critical parameters R_c, $\boldsymbol{k}_c$ and ω_c, and the coefficients in the amplitude and mean drift equations (4.1) for the depth $h = 0.1^{-1/2}$ and the indicated values of the latitude λ and the wind direction θ.

Table 2 shows the critical parameters R_c, $\boldsymbol{k}_c$ and ω_c, and the coefficients in the amplitude equation (4.4) for infinite depth and the indicated values of λ and θ. Also

https://doi.org/10.1017/S0022112002003415 Published online by Cambridge University Press

(λ, θ)	$(90°, -)$	$(40°, 138°)$	$(40°, 180°)$
R_c	31.25	28.08	18.79
$\boldsymbol{k}_c$	(0.36, 0.46)	(0.36, 0.51)	(0.53, 0.45)
ω_c	0.20	0.22	0.16
$\boldsymbol{c}_g$	$(0.24, -0.54)$	$(0.22, -0.51)$	$(0.18, -0.49)$
c_r	$0.03 + 0.07\,\mathrm{i}$	$0.03 + 0.08\,\mathrm{i}$	$0.04 + 0.05\,\mathrm{i}$
c_{11}	$0.26 - 0.10\,\mathrm{i}$	$0.26 - 0.13\,\mathrm{i}$	$0.28 - 0.16\,\mathrm{i}$
c_{12}	$-0.12 + 0.03\,\mathrm{i}$	$-0.12 + 0.05\,\mathrm{i}$	$-0.11 + 0.15\,\mathrm{i}$
c_{21}	$-0.12 + 0.03\,\mathrm{i}$	$-0.12 + 0.05\,\mathrm{i}$	$-0.11 + 0.15\,\mathrm{i}$
c_{22}	$0.21 + 0.05\,\mathrm{i}$	$0.21 + 0.03\,\mathrm{i}$	$0.11 - 0.12\,\mathrm{i}$
c_1	$0.06 - 6.85\,\mathrm{i}$	$0.15 - 6.91\,\mathrm{i}$	$0.14 - 4.04\,\mathrm{i}$
c_2	$-0.07 + 6.13\,\mathrm{i}$	$-0.07 + 5.71\,\mathrm{i}$	$-0.19 + 5.53\,\mathrm{i}$
c_a	$0.27 + 0.26\,\mathrm{i}$	$0.34 + 0.32\,\mathrm{i}$	$0.34 + 0.52\,\mathrm{i}$
f_1	0.03	0.03	0.08
f_2	−0.03	−0.03	−0.04

TABLE 1. Parameter values for depth $h = 0.1^{-1/2}$ and selected values of λ and θ.

(λ, θ)	$(90°, -)$	$(40°, 81°)$	$(40°, 231°)$
R_c	11.82	15.49	13.04
$\boldsymbol{k}_c$	(0.25, 0.20)	(0.15, 0.19)	(0.23, 0.38)
ω_c	0.18	0.19	0.26
$\boldsymbol{c}_g$	$(0.27, -0.36)$	$(0.09, -0.29)$	$(0.22, -0.29)$
c_r	$0.04 - 0.04\,\mathrm{i}$	$0.03 - 0.03\,\mathrm{i}$	$0.06 - 0.03\,\mathrm{i}$
c_{11}	$0.37 - 0.13\,\mathrm{i}$	$1.08 - 0.58\,\mathrm{i}$	$0.63 + 0.02\,\mathrm{i}$
c_{12}	$-0.27 + 0.04\,\mathrm{i}$	$-0.72 + 0.95\,\mathrm{i}$	$-0.47 + 0.17\,\mathrm{i}$
c_{21}	$-0.27 + 0.04\,\mathrm{i}$	$-0.72 + 0.95\,\mathrm{i}$	$-0.47 + 0.17\,\mathrm{i}$
c_{22}	$0.44 - 0.13\,\mathrm{i}$	$0.70 - 1.31\,\mathrm{i}$	$0.42 - 0.32\,\mathrm{i}$
c_a	$0.04 + 0.07\,\mathrm{i}$	$0.02 + 0.04\,\mathrm{i}$	$0.12 + 0.07\,\mathrm{i}$
b_1	−0.70	−2.15	−1.51
b_2	−0.25	0.25	0.51
c	1.90	1.79	0.55
s_t	5.24	6.13	13.75
H_{11}	13.59	4.74	24.56
H_{12}	11.36	13.87	43.29
H_{21}	−4.27	−12.81	−32.05
H_{22}	6.54	−9.71	−24.33
s_a	0.93	0.89	0.52
s_ω	−0.90	−1.32	−0.48

TABLE 2. Parameter values for infinite depth and selected values of λ and θ.

shown are the parameters b_1, b_2 and c in the amplitude equation in irreducible form (4.6) and the transformation parameters in (4.5).

Appendix B. Derivation of the amplitude equations

In the perturbation analysis the variables are expanded as follows:

$$\partial_\mu \to \partial_\mu + \epsilon\partial_{X_\mu}, \quad \partial_t \to \partial_t + \epsilon\partial_{T_1} + \epsilon^2\partial_{T_2}, \tag{B 1a}$$

$$\chi = \epsilon\chi^{(1)} + \epsilon^2\chi^{(2)}, \quad \psi = \epsilon\psi^{(1)} + \epsilon^2\psi^{(2)}, \tag{B 1b}$$

$$G_\mu = \epsilon^2 G_\mu^{(2)}, \quad G_3 = \epsilon^3 G_3^{(3)}, \tag{B 1c}$$

https://doi.org/10.1017/S0022112002003415 Published online by Cambridge University Press

where T_1, T_2 and X_μ are 'slow variables'. The first-order function $\chi^{(1)}$ is assumed to have the form

$$\chi^{(1)} = A(T_1, T_2, X_\mu)\ \hat{\chi}^{(1)}(x_3)\ \exp(\mathrm{i}\,\boldsymbol{k}_c \cdot \boldsymbol{x} + \mathrm{i}\,\omega_c t) + \text{c.c.}, \tag{B 2}$$

and similarly for $\psi^{(1)}$. The normalization of $\hat{\chi}^{(1)}$ and $\hat{\psi}^{(1)}$ is chosen so that

$$\int_{-h}^{0} \left|\hat{v}_1^{(1)}\right|^2 + \left|\hat{v}_2^{(1)}\right|^2 + \left|\hat{v}_3^{(1)}\right|^2 \mathrm{d}x_3 = 1, \tag{B 3}$$

where according to the representation (2.8) $\hat{v}_1^{(1)} = \mathrm{i}\,(\boldsymbol{k}_c \cdot \hat{\boldsymbol{e}}_1)\partial_3 \hat{\chi}^{(1)} + \mathrm{i}(\boldsymbol{k}_c \cdot \hat{\boldsymbol{e}}_2)\hat{\psi}^{(1)}$, etc. Substitution of the expansions (B 1) and (B 2) into equations (2.9) and (2.10) yields linear inhomogeneous equations at every order in the expansion parameter $\epsilon = [(R - R_c)/R_c]^{1/2}$. The critical parameters R_c, $\boldsymbol{k}_c$ and ω_c are chosen such that the linear operator in (2.9) is singular. That operator reappears at every order in ϵ and therefore solvability conditions need to be applied to the inhomogeneous terms. These conditions yield a differential equation for the amplitude A. In the finite depth case that equation is coupled to a Poisson equation for a pressure variable. The derivation of the amplitude equation is standard (Newell & Whitehead 1969; Cross & Hohenberg 1993), and we only give details of the part of the analysis that pertains to the pressure variable.

B.1. *Finite depth*

The pressure is expanded as

$$\pi = \epsilon\left(\pi^{(1)} + \pi_s\right) + \epsilon^2 \pi^{(2)}, \tag{B 4}$$

where π_s only depends on slow variables. The second-order mean momentum equations (2.10) are

$$\begin{aligned} 0 = &-\partial_{X_1}\pi_s + 2\Omega_3 G_2^{(2)} + R^{-1}\partial_{33} G_1^{(2)} \\ &- |A|^2\left\{\mathrm{i}|\boldsymbol{k}_c|^2\partial_3\left(\chi^{(1)*}\partial_3\chi^{(1)}\hat{\boldsymbol{e}}_1 + \chi^{(1)*}\psi^{(1)}\hat{\boldsymbol{e}}_2\right)\cdot\boldsymbol{k}_c + \text{c.c.}\right\}, \quad \text{(B 5}a\text{)} \\ 0 = &-\partial_{X_2}\pi_s - 2\Omega_3 G_1^{(2)} + R^{-1}\partial_{33} G_2^{(2)} \\ &- |A|^2\left\{\mathrm{i}|\boldsymbol{k}_c|^2\partial_3\left(\chi^{(1)*}\partial_3\chi^{(1)}\hat{\boldsymbol{e}}_2 - \chi^{(1)*}\psi^{(1)}\hat{\boldsymbol{e}}_1\right)\cdot\boldsymbol{k}_c + \text{c.c.}\right\}. \quad \text{(B 5}b\text{)} \end{aligned}$$

The solution of (B 5) can be written as

$$G_\mu^{(2)} = \hat{G}_\mu^{(2)}(x_3)\,|A|^2 + \hat{g}_{\mu\nu}^{(2)}(x_3)\,\partial_{X_\nu}\pi_s, \tag{B 6}$$

where the functions $\hat{G}_\mu^{(2)}$ and $\hat{g}_{\mu\nu}^{(2)}$ are easily computed numerically. The term in (B 6) proportional to $|A|^2$ contributes to the cubic term in the amplitude equation in the usual way, whereas the term proportional to $\partial_{X_\nu}\pi_s$ establishes the coupling between the amplitude and the pressure equations. The latter equation is obtained by substitution of (B 6) into the third-order continuity equation

$$\partial_3 G_3^{(3)} = -\partial_{X_\mu} G_\mu^{(2)}, \tag{B 7}$$

and integration of (B 7) from $x_3 = -h$ to $x_3 = 0$ using the boundary conditions $G_3^{(3)}(x_3 = -h) = G_3^{(3)}(x_3 = 0) = 0$. Using the variables $a = \epsilon A$ and $p_s = \epsilon\pi_s$ casts the amplitude and pressure equations into the form (4.1). If the pressure variable π_s were not introduced into the analysis, the boundary condition $G_3^{(3)}(x_3 = -h) = 0$ could not be enforced.

https://doi.org/10.1017/S0022112002003415 Published online by Cambridge University Press

B.2. *Infinite depth*

No slowly varying pressure variable is introduced and the pressure is expanded like the variables χ and ψ in (B 1). The analysis proceeds as in the previous section with $\pi_s = 0$. We introduce a slow vertical variable $X_3 = x_3/h$ and consider the limit $h \to \infty$. $G_3^{(3)}$ is written as

$$G_3^{(3)} = G_3^{(3)(f)}(x_3) + G_3^{(3)(s)}(X_3). \tag{B 8}$$

The function $G_3^{(3)(f)}$ is determined by (B 7) and

$$G_3^{(3)(s)}(X_3 = -1) = -\partial_{X_\mu}|A|^2 \int_{-h}^{0} \hat{G}_\mu^{(2)}(x_3)\,\mathrm{d}x_3. \tag{B 9}$$

Appendix C. Numerical methods and checks

In the computations of the critical parameters and of the coefficients in the amplitude equations, we use the spectral collocation method with Chebyshev polynomials to discretize the computations in the vertical coordinate (Canuto *et al.* 1988). The critical parameters are checked with numerous published results, e.g. Iooss *et al.* (1978), Cox *et al.* (1992), and Leibovich & Lele (1985). We check the computations leading to coefficients c_r and c_a in the amplitude equations (4.1) by comparing the values we obtain for these coefficients in the case of Langmuir circulations (not reported here), with those reported by Cox *et al.* (1992). Furthermore, we check the functions $\hat{\chi}^{(1)}$ and $\hat{\psi}^{(1)}$, multiplied by the homogeneous Stokes wave solution, with results for these functions from a fully nonlinear computation of the convection roll state close to threshold. Finally, we found the stability analysis of the Stokes wave solutions to be consistent with the stability analysis of the fully nonlinear solutions. Unfortunately, a check with the weakly nonlinear analysis reported by Iooss *et al.* (1978) is not entirely successful; for the quantity $(\zeta_{10}/\gamma_r)^{1/2}$ in that paper we obtain the value 1.38, whereas the reported value is 0.90. In the light of the fact that all other checks are successful, we contend that our results are accurate.

For the simulations we use a spectral code with 126 Fourier modes in each direction. We use periodic boundary conditions and random initial conditions. We assign to the value of the amplitude a at every grid point a random number from the interval $[-F, F]$, where F is the magnitude of the uniform Stokes wave solution. Typical simulations are those of case II, for which we use a square box of size 316×316, a constant time step of 0.7 time units and run the code for 140 000 time steps.

REFERENCES

Barcilon, V. 1965 Stability of a non-divergent Ekman layer. *Tellus* **17**, 53–68.

Benjamin, T. B. & Feir, J. E. 1967 The disintegration of wave trains on deep water. Part 1. Theory. *J. Fluid Mech.* **27**, 417–430.

Brown, R. A. 1970 A secondary flow model for the planetary boundary layer. *J. Atmos. Sci.* **27**, 742–757.

Brown, R. A. 1972 On the inflection point instability of a stratified Ekman boundary layer. *J. Atmos. Sci.* **29**, 850–859.

Caldwell, D. R. & Van Atta, C. W. 1970 Characteristics of Ekman layer instabilities. *J. Fluid Mech.* **44**, 79–95.

Caldwell, D. R., Van Atta, C. W. & Helland, V. N. 1972 A laboratory study of the turbulent Ekman layer. *Geophys. Fluid Dyn.* **3**, 125–160.

Canuto, C., Hussaini, M. Y., Quateroni, A. & Zang, T. A. 1988 *Spectral Methods in Fluid Dynamics.* Springer.

https://doi.org/10.1017/S0022112002003415 Published online by Cambridge University Press

Chaté, H. & Manneville, P. 1996 Phase diagram of the two-dimensional complex Ginzburg–Landau equation. *Physica* A **224**, 348–368.

Coleman, G. N., Ferziger, J. H. & Spalart, P. R. 1990 A numerical study of the turbulent Ekman layer. *J. Fluid Mech.* **213**, 313–348.

Coullet, P., Gil, L. & Lega, J. 1989 A form of turbulence associated with defects. *Physica* D **37**, 91–103.

Cox, S. M., Leibovich, S., Moroz, I. M. & Tandon, A. 1992 Nonlinear dynamics in Langmuir circulation with O(2) symmetry. *J. Fluid Mech.* **241**, 669–704.

Cross, M. C. & Hohenberg, P. C. 1993 Pattern formation outside of equilibrium. *Rev. Mod. Phys.* **65**, 851–1112.

Davey, A., Hocking, L. M. & Stewartson, K. 1974 On the nonlinear evolution of three-dimensional disturbances in plane Poiseuille flow. *J. Fluid Mech.* **63**, 529–536.

Deardorff, J. W. 1972 Numerical investigation of neutral and unstable planetary boundary layers. *J. Atmos. Sci.* **29**, 91–115.

Ekman, V. W. 1905 On the influence of the Earth's rotation on ocean currents. *Arkiv für Matematik, Astronomi Och Fysik* **2**, 1–53.

Etling, D. 1971 The stability of an Ekman boundary layer flow as influenced by the thermal stratification. *Beitr. Phys. Atmos.* **44**, 168–186.

Etling, D. & Wippermann, F. 1975 On the instability of a planetary boundary layer with Rossby-number similarity. *Boundary-layer Met.* **9**, 341–360.

Faller, A. J. 1963 An experimental study of the instability of the laminar Ekman boundary layer. *J. Fluid Mech.* **15**, 560–576.

Faller, A. J. 1964 The angle of windrows in the ocean. *Tellus* **16**, 363–370.

Faller, A. J. & Kaylor, R. E. 1966*a* Investigations of stability and transition in rotating boundary layers. In *Dynamics of Fluids and Plasmas* (ed. S. I. Pai), pp. 309–329. Academic.

Faller, A. J. & Kaylor, R. E. 1966*b* A numerical study of the instability of the laminar Ekman boundary layer. *J. Atmos. Sci.* **23**, 466–480.

Faller, A. J. & Kaylor, R. E. 1967 Instability of the Ekman spiral with applications to the planetary boundary layer. *Phys. Fluids Suppl.* **10**, 212–219.

Greenspan, H. P. 1968 *The Theory of Rotating Fluids.* Cambridge University Press.

Haeusser, T. M. 1998 Pattern formation in the oceanic Ekman–Langmuir layer. PhD thesis, Cornell University, 137 pp.

Haeusser, T. M. & Leibovich, S. 1997 Amplitude and mean drift equations for the oceanic Ekman layer. *Phys. Rev. Lett.* **79**, 329–332.

Hoffmann, N. P. 1997 Beiträge zur Theorie der Ekman-Schicht. PhD thesis, Universität Bayreuth, 121 pp.

Iooss, G., Nielsen, H. B. & True, H. 1978 Bifurcation of the stationary Ekman flow into a stable periodic flow. *Arch. Rat. Mech. Anal.* **68**, 227–256.

Joseph, D. 1976 *Stability of Fluid Motions.* Springer.

Leibovich, S. 1983 The form and dynamics of Langmuir circulations. *Annu. Rev. Fluid Mech.* **15**, 391–427.

Leibovich, S. & Lele, S. K. 1985 The influence of the horizontal component of the Earth's angular velocity on the instability of the Ekman layer. *J. Fluid Mech.* **150**, 41–87.

Lilly, D. K. 1966 On the instability of Ekman boundary flow. *J. Atmos. Sci.* **23**, 481–494.

Mason, P. J. & Thomson, D. J. 1987 Large-eddy simulations of the neutral-static-stability planetary boundary layer. *Q. J. R. Met. Soc.* **113**, 413–443.

Melander, M. V. 1983 An algorithmic approach to the linear stability of the Ekman layer. *J. Fluid Mech.* **132**, 283–293.

Newell, A. C. & Whitehead, J. A. 1969 Finite bandwidth, finite amplitude convection. *J. Fluid Mech.* **38**, 279–303.

Shraiman, B. I., Pumir, A., Van Saarloos, W., Hohenberg, P. C., Chaté, H. & Holen, M. 1992 Spatiotemporal chaos in the one-dimensional complex Ginzburg–Landau equation. *Physica* D **57**, 241–248.

Smith, J. A. 1996 Observations of Langmuir circulation, waves, and the mixed layer. *Proc. Symposium on the Air-Sea Interface, Marseilles 1993* (ed. M. Donelan, W. H. Hui & W. J. Plant). Rosenstiel School of Marine and Atmospheric Science, University of Miami.

https://doi.org/10.1017/S0022112002003415 Published online by Cambridge University Press

Spooner, G. F. 1983 Stability of free surface Ekman layers. *J. Phys. Oceanogr.* **13**, 663–677.

Spooner, G. F. & Criminale, W. O. 1982 The evolution of disturbances in an Ekman boundary layer. *J. Fluid Mech.* **115**, 327–346.

Stern, M. E. 1960 Instability of the Ekman layer at large Taylor number. *Tellus* **12**, 399–417.

Tatro, P. R. & Mollo-Christensen, E. L. 1967 Experiments on Ekman layer instability. *J. Fluid Mech.* **28**, 531–543.

Weber, A., Bodenschatz, E. & Kramer, L. 1991 Defects in continuous media. *Adv. Mater.* **3**, 191–197.

Wippermann, F. 1969 The orientation of vortices due to instability of the Ekman boundary layer. *Beitr. Phys. Atmos.* **48**, 30–45.

Wippermann, F., Etling, D. & Kirstein, H. J. 1978 On the instability of a planetary boundary layer with Rossby number similarity. Part II. The combined effect of inflection point instability and convective instability. *Boundary-Layer Met.* **15**, 301–321.

https://doi.org/10.1017/S0022112002003415 Published online by Cambridge University Press